npj | Materials Degradation

www.nature.com/npjmatdeg

ARTICLE OPEN

Deciphering the degradation mechanism of the lead-free all inorganic perovskite Cs_2SnI_6

Weiguang Zhu[1], Guoqing Xin[1], Spencer M. Scott[1], Wenqian Xu[2], Tiankai Yao[1], Bowen Gong[1], Yachun Wang[1], Mingxin Li[1] and Jie Lian[1]

Organic-inorganic perovskite materials are revolutionizing photovoltaics with high power conversion efficiencies, but experience significant environmental degradation and instability. In this work, the phase stability and decomposition mechanisms of lead-free all inorganic Cs_2SnI_6 perovskite upon water and moisture exposure were systematically investigated via in situ synchrotron X-ray diffraction, environmental SEM, and micro-Raman spectroscopy. A critical relative humidity (80%) is identified below which Cs_2SnI_6 perovskite is stable without decomposition. Under higher humidity or aqueous environment, Cs_2SnI_6 perovskite decomposes into SnI_4 and CsI through etch pits formation and stepwave propagation, leading to rapid crystal dissolution. A partial reversibility of the Cs_2SnI_6 perovskite upon dissolution and re-precipitation with subsequent dehydration was identified, suggesting a self-healing capability of Cs_2SnI_6 and thus enhanced air stability. Mechanistic understanding of the Cs_2SnI_6 degradation behavior can be a vital step towards developing new perovskites with enhanced environmental stability and materials performance.

npj Materials Degradation (2019)3:7 ; https://doi.org/10.1038/s41529-019-0068-3

INTRODUCTION

Organic–inorganic perovskites have attracted significant attention from researchers in recent years due to their impressive properties for photovoltaic applications, including high absorption coefficients, long carrier diffusion length, and solution processability,[1–4] boosting the photovoltaic power conversion efficiency (PCE) over 20%.[5–7] Despite endeavors to optimize cell design and achieve excellent device efficiencies, technical barriers to the implementation of perovskite solar cells remain such as the toxicity of lead, and the long-term environmental instability of perovskite compositions.[8] Particularly, the organic–inorganic hybrid perovskite ($CH_3NH_3PbI_3$) undergoes a rapid decomposition to PbI_2 in the presence of moisture, resulting in a substantial decrease of the device performance.[9–13] It suffers an 80% drop in PCE over a 24 h period and retains less than 5% after 6 days when the cells were stored in ambient conditions.[9]

In order to address the critical issues of environmental toxicity of Pb and the associated instability, Cs_2SnI_6 has been explored as an alternative lead-free perovskite, which displays high degree of air stability at room temperature due to the oxidation state of Sn^{4+}.[14–16] In addition to the air stability, Cs_2SnI_6 has a direct band gap of ~1.3 eV and high absorption coefficient (over 10^5 cm^{-1}).[14,15] It has been successfully adopted as a lead-free light absorber material for solar cells and can retain over 90% in PCE for over 30 days in air.[17] However, the achieved PCE of Cs_2SnI_6 is relatively low (~1%) in air, as compared with $CsSnI_3$ solar cells fabricated under tightly controlled environments,[15,17] and therefore device engineering may be required to further improve the PCE. Due to the conditions expected in the deployment of solar cells, it is vital to understand the moisture stability and the interaction behaviors of Cs_2SnI_6 with water or moisture. Previous work indicates that Cs_2SnI_6 is stable in ambient conditions with low relative humidity (RH) (30–50% RH), and can be stored in ambient conditions for over 2 months without obvious decomposition.[16] However, this material is still susceptible to rapid decomposition upon exposure to high humidity or aqueous conditions. A mechanistic understanding of the degradation process of the lead-free all inorganic perovskite has yet to be achieved.

In this work, we report a systematic investigation of the perovskite's degradation processes via in situ techniques with a goal of elucidating the underlying mechanisms governing their environmental stability. Through a careful control of RH, the morphological changes were monitored using in situ environmental scanning electron microscope (SEM). The dissolution process occurred through the formation of etch pits and subsequent generation of etching steps due to the propagation of the etch pits through the bulk crystal. Interestingly, the well-shaped octahedra crystals recrystallized with the evaporation of water or dehydration, indicating a strong self-healing capability of Cs_2SnI_6. Variations in crystallinity and phase transformations were characterized by in situ micro-Raman spectroscopy and synchrotron X-ray powder diffraction (XRD), indicating a phase decomposition of Cs_2SnI_6 into CsI and SnI_4. The improved understanding of perovskite environmental stability and degradation maybe useful for optimization of the materials preparation and further development of new types of perovskite with enhanced materials performance and environmental stability.

RESULTS AND DISCUSSION

To investigate the underlying mechanisms governing the environmental stability of Cs_2SnI_6, in situ environmental SEM was performed to observe the microstructural evolution at the micro- and/or nanoscale. Figure 1 shows the in situ environmental

[1]Department of Mechanical, Aerospace and Nuclear Engineering, Rensselaer Polytechnic Institute, Troy, NY 12180, USA and [2]X-ray Science Division, Advanced Photon Source, Argonne National Laboratory, Lemont, IL 60439, USA
Correspondence: Jie Lian (lianj@rpi.edu)

Received: 16 August 2018 Accepted: 10 January 2019
Published online: 15 February 2019

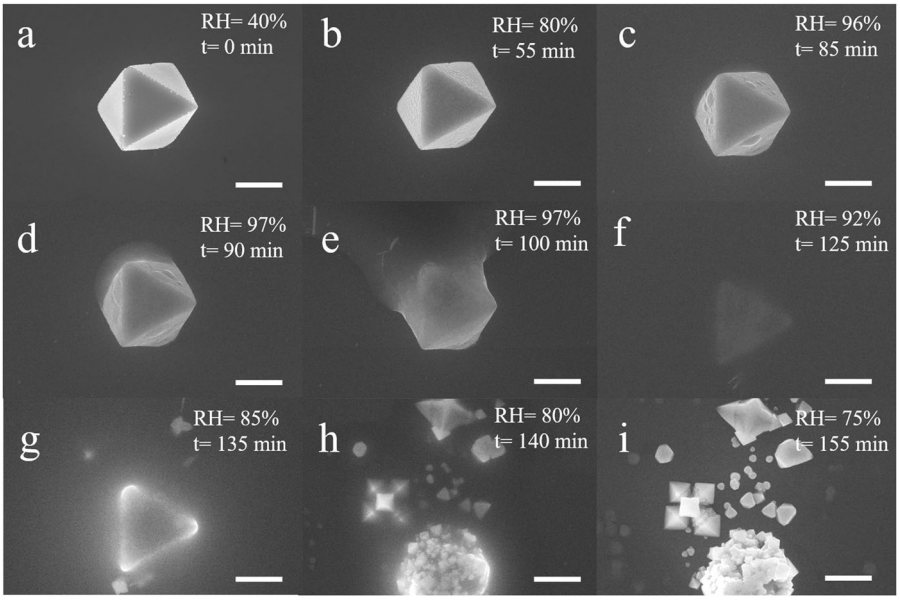

Fig. 1 Dissolution and recrystallization process. **a**–**f** The dissolution process of a Cs_2SnI_6 crystal under increasing relative humidity. **g**–**i** The recrystallization process upon reducing water vapor pressure. The scale bar is 5 μm

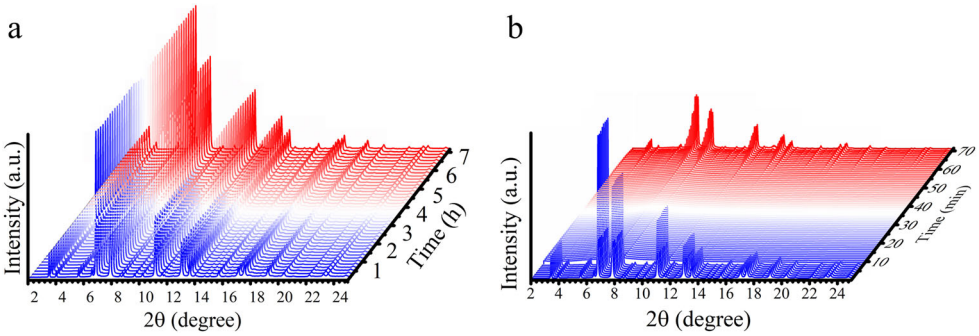

Fig. 2 In situ synchrotron X-ray diffraction patterns of Cs_2SnI_6 powders **a** exposed to ~80% RH environment at room temperature and **b** with water drops added on the sample

SEM images of the dissolution and recrystallization processes of a Cs_2SnI_6 crystal upon controlling the water vapor pressure (also see Supplementary Information; Supplementary Video S1). The as-prepared Cs_2SnI_6 had a crystallite size ~10 μm with an octahedral shape, and was placed on an Si substrate held at 15 °C (Fig. 1a). The RH in the chamber was controlled by a leak valve. As the water vapor pressure increased, the well-facet Cs_2SnI_6 crystal was maintained—even after increasing an RH to 80% in 55 min, as shown in Fig. 1b. To further confirm the phase stability in moist air, the interaction of Cs_2SnI_6 with water vapor was monitored by in situ synchrotron X-ray powder diffraction under high humidity (~80%) at room temperature. For an exposure period in excess of 7 h, in situ XRD of Cs_2SnI_6 powders suggests the retention of the perovskite structure, with no decomposition peaks visible, as shown in Fig. 2a. This demonstrates that Cs_2SnI_6 is stable in the moist air, up to 80% RH, which is consistent with the results obtained during in situ environmental SEM and results reported previously.[14,18,19]

It should be noted that small dots emerged on the crystal surface, appearing at 45% and disappearing at ~60%. These dots are believed to be Cs_2SnI_6 quantum dots formed during the synthesis process. As pointed out from our previous report,[16] Cs_2SnI_6 has significant solubility in many common organic solvents, such as ethanol, methanol, and dimethylformamide. The synthesis process in this work utilized methanol and n-butyl acetate organic solvents. Due to the solubility of Cs_2SnI_6 in these organic solvents, it is highly possible that small particles re-precipitated on the crystal surface during the drying process, as observed from the original powder (Fig. 1a). In addition, Cs_2SnI_6 powders prepared using ethanol in the place on n-butyl acetate displayed numerous small particles precipitates on powders (Fig. S1). Despite the presence of these small particles across preparation techniques, all of the Cs_2SnI_6 powders in this study have not displayed any impurities in the XRD characterization. Similarly, Kapil et al.[20] previously reported the presences of quantum dots formed on the bulk Cs_2SnI_6 material. Therefore, the small dots observed in our in situ experiment are likely quantum dots of Cs_2SnI_6. These small particles would easily absorb water vapor due to their high surface energy, showing high brightness. As the RH increased to ~60%, these dots disappeared, indicating their preferential dissolution when the particle size is reduced to the nano-metered scale.

Further increments of the water vapor pressure and relatively humidity to 95% resulted in increasingly rough surfaces of the Cs_2SnI_6 crystals with small hillocks formed as a result of the water vapor condensation. The dissolution process began at preferential sites instead of a uniform dissolution on the 3D crystals. The hillocks grew to a shape of small water drops and evolved into larger droplets on the surface as the RH increased to saturated water vapor condition. Under the saturated environment, the

droplets can no longer be held on the surface and instead flow on the substrate, forming a solution around the crystal (Fig. 1c–e). Figure 1f shows the triangle-shaped residue in the dissolved solution after the crystal was held in saturated water vapor (RH > 95%) for over 30 min, suggesting a nearly complete dissolution of the original Cs_2SnI_6 perovskite. A reversible reaction occurs between Cs_2SnI_6 and water (Fig. 1f–i) with the evaporation of water molecules to ~85% RH. The residue could act as nucleation sites from which well-shaped octahedral crystals precipitate and grow.

The degradation behavior and reversible reaction of Cs_2SnI_6 with water were also confirmed using in situ synchrotron X-ray diffraction (XRD), as shown in Fig. 2b. Once Cs_2SnI_6 was exposed to water, the diffraction peaks of Cs_2SnI_6 perovskite decreased rapidly. Within 10 min of water exposure, the powder was fully dissolved, and no obvious crystallinity was observed (Fig. S2). Interestingly, as the water evaporated, the diffraction patterns which can be assigned to Cs_2SnI_6 reappeared, suggesting Cs_2SnI_6 re-precipitated from the solution (Figs 2b and S2). It is worth noting the recovered diffraction intensity of Cs_2SnI_6 is lower than the original one, indicating a partial recovery process. These results indicate a critical humidity (~80% RH) exists below which the decomposition of Cs_2SnI_6 will not occur and the material remains stable. The reversible reaction also suggests a strong self-healing capability of the Cs_2SnI_6 perovskite upon dehydration, providing strong evidence of the enhanced environmental stability as compared with organic–inorganic hybrid perovskite.[11,21,22]

Detailed mechanisms of the dissolution process were further analyzed using ex situ SEM observation, in which the formation of etch pits and dissolution surface steps were visible. In the dissolution stepwave model, the surface defects, e.g., surface steps or edge dislocations, act as the energetically favorite sites for crystal dissolution. Figure 3a shows the fine octahedral shape of Cs_2SnI_6 crystals displaying a layered structure with clearly visible growth steps, indicating the layer-by-layer growth into the bulk crystal. These surface steps and dislocations introduce strain energy into the crystal, which is energetically favorable to the formation of etch pits.[23] The dislocation strain energy can be calculated by the following equation[24]:

$$u(r) = \frac{\mu b^2/(8\pi^2)}{r_h^2 + r^2}, \quad (1)$$

where μ is the isotropic bulk shear modulus (egs/cm^3), b is the size of the Burgers vector (Å), r_h (Å) and r (Å) are the size of the hollow core and the distance from the dislocation center, respectively. Based on this equation, the center of the initial dislocation defects has a higher strain energy, and therefore the dissolution process moves away from the center and travels across the crystal surface, generating etch pits. Further etch steps can be generated from the step far from the center of the dislocation, and the continuous movement of these steps into the crystal will form a series of steps, based on the dissolution stepwave model.[23,25] The stepwaves from each etch pit combine to lower the crystal surface area (Fig. 3b), controlling the bulk crystal dissolution rate. With the continuous dissolution, the etch pits grow in both the vertical and horizontal directions, resulting in a drop in the surface and hollow holes in the crystals as shown in Fig. 3b, c. Figure 3d displays a schematic view of the dissolution model highlighting the formation mechanism of etch pits and the combination of stepwaves resulting in the overall crystal dissolution.

The etch pits and stepwave dissolution mechanism are more clearly visible when Cs_2SnI_6 was treated with methanol. Cs_2SnI_6 has a lower solubility in methanol as compared to water. It is more evident that the dissolution process of Cs_2SnI_6 involved the formation of etch pits and the combination of stepwaves from each etch pit eventually leads to the hollow structure of Cs_2SnI_6 crystals. Figure 4a shows that the triangle etch pits are visible and surrounded by relatively-flat surfaces while exposed to methanol. The stepwaves from these etch pits combined and formed larger pits during the dissolution process (Fig. 4b). The larger pits eventually formed a large hollow pit in the crystal with the etch pits propagating perpendicularly through the bulk crystal, as shown in Fig. 4c. A close look at the etch pit suggests that the dissolution process proceeds along the <111> direction, forming a hexagonal dissolution pit.

Figure 5 shows SEM images of various locations on the substrate after the recrystallization process, indicating the partial reversibility of the process. In Fig. 5a, multiple octahedral crystals can be observed with a hollow structure, which are not fully dissolved under the saturated condition. These residual crystals may act as new nucleation sites during the recrystallization process, as evidenced by the presence of small crystals on the surface (Fig. 5a). During the dissolution process, water condensed on the substrate and formed droplets containing decomposition

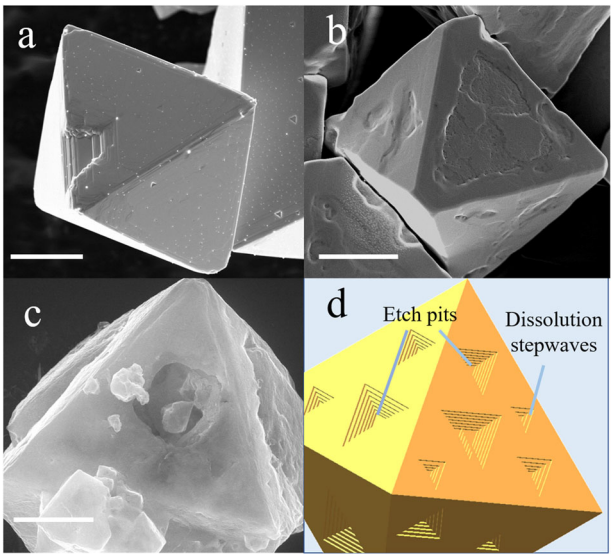

Fig. 3 **a** As-prepared Cs_2SnI_6 crystals, exhibiting the layered structure and lots of surface defects. **b** The combing etch pits, lowering the entire crystal surface. **c** The pit formation in the Cs_2SnI_6 crystal. Scale bars are 5 μm. **d** The schematic graph of the formation of etch pits and the stepwaves from both etch pits combine, leading to a drop of the crystal surface

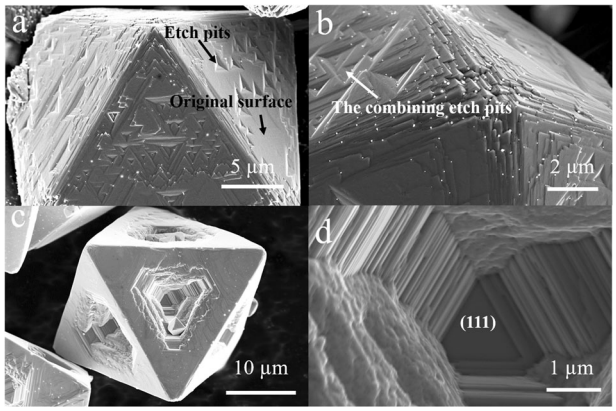

Fig. 4 **a** Etch pits obtained with methanol, which presents well-shaped triangles. **b** SEM image of the combing etch pits. **c** The etched Cs_2SnI_6 crystal with a hollow structure. **d** A high magnification SEM image of the pitting, indicating dissolution along <111> directions

products. As the water evaporated, perovskite crystals re-precipitated out, forming a ring-like pattern that consisted of small crystals, as shown in Fig. 5b. It was observed that crystals on the edge are larger than the central crystals. This may be explained by a phenomenon known as a coffee ring effect,[26] which is caused by capillary flow from the interior to the edge due to the differential evaporation rate. Dendrites and needle-like precipitates were also observed throughout the sample, reinforcing the partial reversibility of Cs_2SnI_6 and the dissolution–precipitation mechanism (Fig. 5c, d). A similar partially reversible process resulting from water interaction has also been reported in the organic–inorganic perovskite.[13,22,27]

Synchrotron X-ray powder diffraction was used to analyze the phase compositions of the re-precipitated materials after the water was evaporated. As shown in Fig. 6a, the Cs_2SnI_6 perovskite phase is clearly visible at different locations, confirming the self-healing capability and reversible reaction with water. In addition, SnI_4 was also identified at P1, suggesting the process is not entirely reversible. Rietveld refinement of the precipitated products indicates that the phase fraction of Cs_2SnI_6 and SnI_4 are 55% and 45%, respectively (Fig. S3). Besides, CsI could also be identified at P2 and P3. Therefore, synchrotron XRD confirms coexistence of recrystallized Cs_2SnI_6, and residual decomposition products CsI and SnI_4 aggregated at different regions. The CsI precipitated as large sized crystals, characterized by the diffraction spots shown in Fig. 6b. Post experiment SEM images indicate that small particles deposited on and around the recrystallized Cs_2SnI_6 could be SnI_4. Large dendrites were also observed similar with the in situ environmental SEM results, which may be CsI (Fig. S4). The broad peak at 2θ ~5° is attributed to the formation of $Sn(OH)_4$, the product of the hydrolysis of SnI_4.

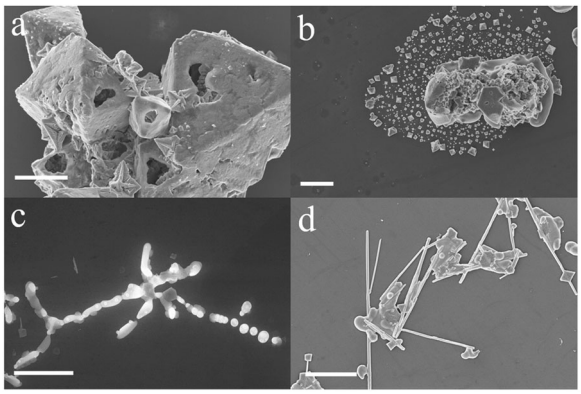

Fig. 5 **a** The partially dissolved Cs_2SnI_6 crystal with a hollow structure, acting as nucleation sites. **b** The reprecipitates formed around the residual crystal. **c** The dissolved product precipitated and formed dendrites. **d** The needle-like structure formed from the dissolution products

In situ Raman and optical images were also performed to further reveal the phase decomposition and precipitation processes of Cs_2SnI_6 perovskite interacting with water. Figure 7a displays optical images of Cs_2SnI_6 powders upon the addition of water, indicating that Cs_2SnI_6 can decompose rapidly upon exposure to water. Cs_2SnI_6 underwent a color change from black to a yellow solution and eventually a yellow slurry. The reversibility of the dissolution–precipitation process was further supported by these color changes, with the color change from yellow to black upon drying at room temperature (Fig. 7a).

Figure 7b displays micro-Raman spectra obtained at various times after exposing Cs_2SnI_6 powders to water. The starting Cs_2SnI_6 powders had an average crystallite size around 15 μm with a well-defined octahedral shape, as shown in Fig. 7c. For the as-prepared Cs_2SnI_6 powders, a sharp band at 126 cm^{-1} and two weak bands at 77 and 248 cm^{-1} were observed. The band at 126 cm^{-1} can be attributed to the Sn-I stretching vibration ν (A_{1g}). The low frequency band at 77 cm^{-1} can be ascribed to the δ (F_{2g}) mode involving I-Sn-I asymmetric bending.[28] With the addition of several water droplets, the Cs_2SnI_6 powders began to decompose and dissolve in water. The Raman spectrum obtained at 15 min shows broad bands at 108 and 580 cm^{-1}, which may be attributed to $Sn(OH)_4$[29] as a result of the hydrolysis reaction of SnI_4. Further dissolution results in enhanced signal from decomposition products, further evidenced by a greater number of crystals formed at the bottom, consistent with the sharper peaks of Raman spectrum collected at 25 min. As water evaporated, Cs_2SnI_6 crystals re-precipitated from the solution as shown in Fig. 7b. In addition, the strong peak at 145 cm^{-1} emerged due to the presence of SnI_4, consistent with the findings from synchrotron XRD diffraction (Fig. 6a). The strong variation in color between the two compositions, the black crystal is Cs_2SnI_6 and the orange particles are SnI_4, enabling their identification via optical microscopy in Fig. 7f.

Optical images shown in Fig. 8a display the decomposition of Cs_2SnI_6 in water, as evidenced by the white gel-like precipitates which are the result of a hydrolysis reaction forming tin (IV) hydroxide. Changes in the pH value suggest a strong acid solution arising from the formation of hydriodic acid (Fig. 8c) associated with the hydrolysis reaction (reaction 3). A similar phenomena was observed in a prior tin (IV) iodide hydrolysis experiment.[30] After 12 h, the transparent solution turned yellow, indicating the presence of molecular iodine in the solution (Fig. 8b). The formation of molecular iodine may be attributed to the decomposition product of hydrogen iodide. Based on the systematic in situ measurements of phases, morphology evolution and

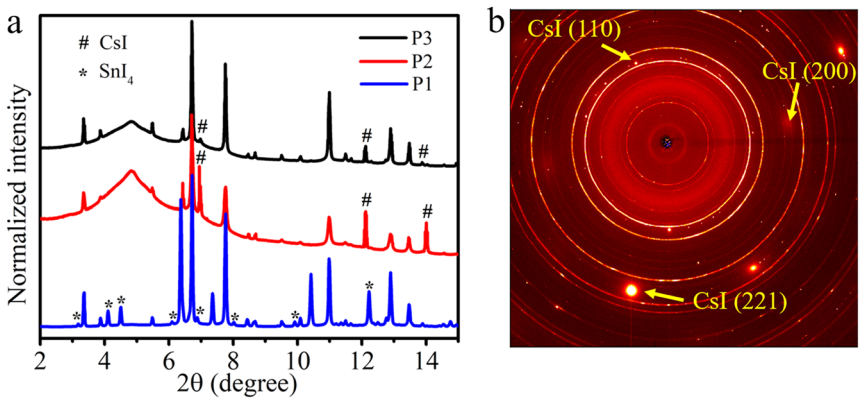

Fig. 6 **a** Phase identification of the re-precipitation products after dehydration and water evaporation by synchrotron X-ray diffraction at different locations (i.e. P1, P2, P3). **b** The synchrotron XRD 2D pattern displaying CsI precipitate

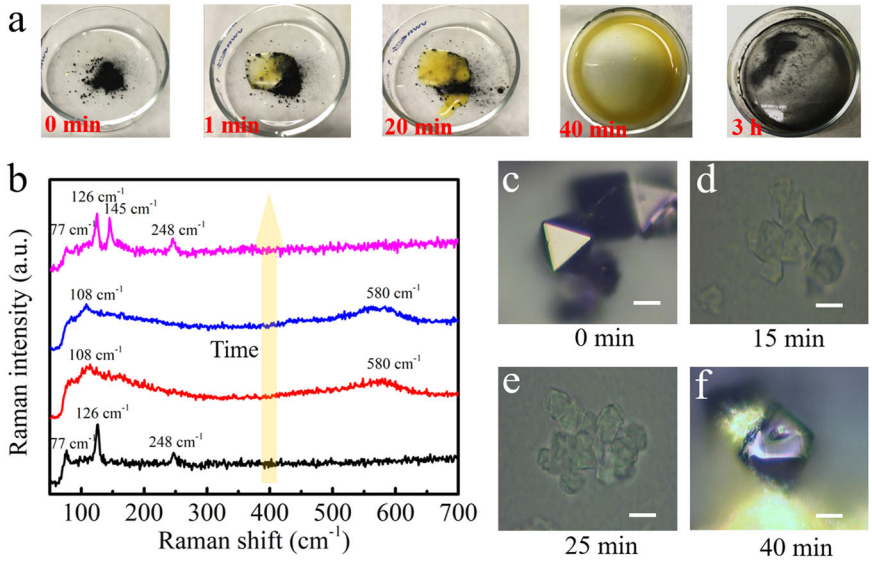

Fig. 7 **a** Color changes of Cs_2SnI_6 powder during hydrating and dehydrating processes. **b** Micro-Raman spectra for Cs_2SnI_6 crystals interaction with water at various time. Spectra from bottom to top are collected at 0, 15, 25, and 40 min, respectively. The corresponding micrographs at **c** 0 min, **d** 15 min, **e** 25 min, and **f** 40 min, respectively. The scale bars are 10 μm

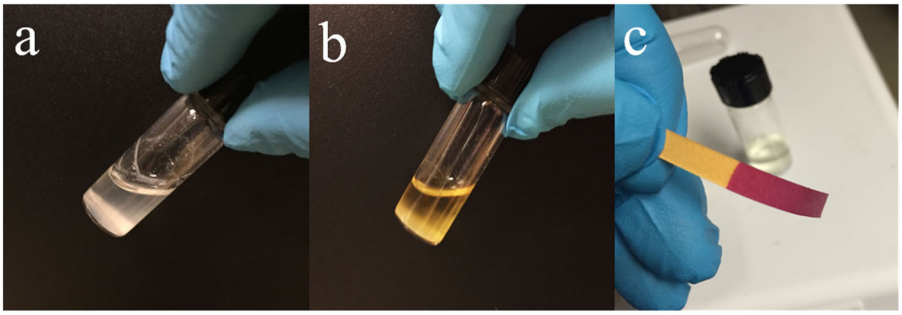

Fig. 8 **a** The fully dissolved Cs_2SnI_6 in water with white gel-like precipitate. **b** The solution turned yellow after placed for over 12 h. **c** The dissolved solution tested by PH strips, indicating the strong acid solution

solution chemistry, the dissolution and recrystallization mechanism of the lead-free all inorganic Cs_2SnI_6 perovskite upon water interaction can be expressed as follows:

$$Cs_2SnI_6 \leftrightarrow SnI_4 + 2CsI, \quad (2)$$

$$SnI_4 + 4H_2O \leftrightarrow Sn(OH)_4 + 4HI, \quad (3)$$

Finally, the degradation behavior of Cs_2SnI_6 was compared to the organic–inorganic perovskite ($MAPbI_3$ or $CH_3NH_3PbI_3$) to further improve the general understanding of perovskite degradation mechanisms. For $MAPbI_3$ perovskite, during the reversible hydration process, water molecules are incorporated into the crystal structure, forming the monohydrate ($CH_3NH_3PbI_3{\cdot}H_2O$).[22,31,32] With prolonged water vapor exposure, it forms the dihydrate, $(CH_3NH_3)_4PbI_6{\cdot}2H_2O$), leading to an irreversible degradation of $MAPbI_3$ perovskite.[22,32] The water molecule intercalation into the crystal structure induces the distortion of the 3D $MAPbI_3$ perovskite structure and rearrangement, resulting in a separation of the $[PbI_6]^{4-}$ octahedra to form 1D double-chains $MAPbI_3$ perovskite species or 0D frameworks.[22] However, in the Cs_2SnI_6 perovskite no hydrated phases have been observed. This may be explained by the higher hydration energy of the Cs^+ cation (−67.7 kcal/mol),[33] as compared to the $CH_3NH_3^+$ cation (−75 kcal/mol).[34] In addition, due to the high ionic mobility of Cs^+ cation in water,[35] Cs^+ cations may diffuse out more rapidly upon exposure to water resulting in the dissociation of the Cs_2SnI_6 perovskite crystal structure, rather than forming the hydrates. The Sn^{4+} is stable in the ambient condition, but experiences the hydrolysis in the water. Therefore, the enhanced moisture stability of Cs_2SnI_6 as compared with that of the organic–inorganic perovskite may be a result of synergistic effects from both Cs^+ and Sn^{4+}, and more investigations are needed to determine the relative contributions of Cs, Sn, and I to the stability.

In summary, this work investigated the degradation process of Cs_2SnI_6 perovskite under controlled RH environment or aqueous conditions via in situ measurements, such as in situ environmental SEM, in situ synchrotron XRD, and Raman spectroscopy. The results demonstrate that Cs_2SnI_6 is stable below a critical relatively humidity of 80%, but experiences degradation when exposed to moisture in excess of 80% RH or aqueous conditions. The degradation process of Cs_2SnI_6 was attributed to etch pit formation on the surface of crystals, resulting in the dissolution of the entire crystal as explained by the stepwave model. Through in situ synchrotron XRD and micro-Raman spectroscopy, it was determined that Cs_2SnI_6 decomposes into CsI and SnI_4 in water as evidenced by the formation of the hydrolysis product $Sn(OH)_4$ in the solution. These results may elucidate the fundamental decomposition pathways of Cs_2SnI_6 perovskite governing the stability of halide perovskite.

METHODS

Materials

Unless stated otherwise, all materials and solvents are used as-purchased without further purification. Cesium iodide (CsI, 99.9%), n-butyl acetate (99% min), and hydroiodic acid (HI, 55–58%) were purchased from Alfa Aesar. Tin powder (Sn, ≥99%) and Iodine (I_2, ≥99.99%) were from Sigma Aldrich.

Cs_2SnI_6 preparation

The method follows as previous reported.[16] Typically, CsI (1 mmol) was dissolved in 10 mL methanol and heated to ~60 °C in a water bath. In a separated 25 mL beaker, SnI_4 (0.5 mmol) was dissolved in 4 mL n-butyl acetate with addition of 2 mL hydroiodic acid. Addition of the acid SnI_4 solution to the warm CsI solution under vigorous stirring led to spontaneous precipitation of a fine black powder. The mixture was stirred for a further 30 min to ensure completion of the reaction in the 60 °C water bath. Then the solid was washed by n-butyl acetate twice via centrifuging and dried in an oven at 80 °C overnight at ambient conditions.

In situ environmental SEM test

Environmental SEM (FEI, Versa 3D Dualbeam) was used for the in situ analysis of the dissolution and recrystallization process of Cs_2SnI_6 via controlling RH. Water vapor was introduced into the chamber through a leak valve. Cs_2SnI_6 crystals were placed on an Si substrate controlled at 15 °C. For the in situ experiment, first the water vapor pressure was set to be around 600 Pa to achieve an RH of ~35%. Then, the pressure was increased at a constant rate (20 Pa/min) to a value 1000 Pa (RH = 58.5%), followed by a rate at 10 Pa/min until reaching 1660 Pa. The pressure was then held for 20 min to allow crystal dissolution. After that, the water vapor pressure was reduced at a constant rate of 10 Pa/min to a value ~715 Pa (RH = 41%). During the experiment, images were captured manually with a speed at every minute or every 30 s as appropriate for the reaction kinetics. Without further notification, each image is of the same magnification, taken at the same location.

In situ synchrotron powder diffraction data collection

In situ synchrotron powder XRD was performed at the Advanced Photon Source on beamline 17-BM-B at Argonne National Laboratory using an Si (111) monochromator ($\lambda = 0.39433$ Å). The experiment was carried out by loading approximately 5 mg of powder sample in a Kapton tubing of 1.1 mm diameter. After the diffraction patterns of dry powders were taken, ~250 µL water was added on the powder directly to monitor the degradation process of Cs_2SnI_6 in aqueous condition. It should be noted that after water addition it takes about 5 min before the first pattern obtained (i.e. time between seventh and eighth diffraction pattern), due to the time for restarting the system. The diffraction pattern was recorded by an amorphous silicon-based area detector from PerkinElmer (2048 × 2048, 200 µm pixels). All data were collected at room temperature. To monitor the reaction at real time, the diffraction patterns were continuously collected with 60 s per frame. The obtained patterns were analyzed using the Rietveld refinement functions implemented in GSAS II.[36,37]

In situ micro-Raman spectra were measured on a Renishaw Micro-Raman spectrometer equipped with an Ar+ ion laser ($\lambda = 514.5$ nm) at room temperature. The spectra were collected at every 5 min interval to monitor the interaction between Cs_2SnI_6 and water. A typical spectrum was acquired at an exposure time of 30 s and two accumulations under a power of 20 mW.

To investigate the Cs_2SnI_6 morphology changes before/after the water reaction, SEM was carried out on a Carl Zeiss Supra 55 field emission scanning electron microscope.

DATA AVAILABILITY

The data that support the findings of this study are available from the corresponding author upon reasonable request.

ACKNOWLEDGEMENTS

The synthesis of Cs_2SnI_6 perovskite and dissolution mechanistic understandings were supported as part of the Center for Performance and Design of Nuclear Waste Forms and Containers, an Energy Frontier Research Center funded by the U.S. Department of Energy, Office of Science, Basic Energy Sciences under Award # DE-SC0016584. In situ Synchrotron X-ray diffraction was performed using Beamline 17-BM of the Advanced Photon Source (APS), a US DOE Office of Science User Facility operated for the DOE Office of Science by Argonne National Laboratory under contract no. DE-AC02-06CH11357.

AUTHOR CONTRIBUTIONS

The scope of the experiment was designed by W.Z. and J.L. W.Z. carried out the material synthesis, micro-Raman spectroscopy. G.X. and S.M.S. helped with the sample preparation. W.Z., W.X., T.Y., and B.G. conducted in the in situ synchrotron X-ray diffraction. W.Z. and T.Y. performed in situ environmental SEM and morphology characterization Y.W. was involved in Raman data analysis. M.L. helped draw the schematic graph. W.Z. and J.L. wrote the manuscript. All the authors helped on the paper editing.

ADDITIONAL INFORMATION

Supplementary information accompanies the paper on the *npj Materials Degradation* website (https://doi.org/10.1038/s41529-019-0068-3).

Competing interests: The authors declare no competing interests.

Publisher's note: Springer Nature remains neutral with regard to jurisdictional claims in published maps and institutional affiliations.

REFERENCES

1. Wehrenfennig, C., Eperon, G. E., Johnston, M. B., Snaith, H. J. & Herz, L. M. High charge carrier mobilities and lifetimes in organolead trihalide perovskites. *Adv. Mater.* **26**, 1584–1589 (2014).
2. Xing, G. et al. Long-range balanced electron-and hole-transport lengths in organic-inorganic $CH_3NH_3PbI_3$. *Science* **342**, 344–347 (2013).
3. Jeon, N. J. et al. Solvent engineering for high-performance inorganic–organic hybrid perovskite solar cells. *Nat. Mater.* **13**, 897–903 (2014).
4. Dong, Q. et al. Electron-hole diffusion lengths >175 µm in solution-grown $CH_3NH_3PbI_3$ single crystals. *Science* **347**, 967–970 (2015).
5. Jiang, Q. et al. Planar-structure perovskite solar cells with efficiency beyond 21%. *Adv. Mater.* **29**, 1703852 (2017).
6. Yang, W. S. et al. High-performance photovoltaic perovskite layers fabricated through intramolecular exchange. *Science* **348**, 1234–1237 (2015).
7. Saliba, M. et al. Incorporation of rubidium cations into perovskite solar cells improves photovoltaic performance. *Science* **354**, 206–209 (2016).
8. Hodes, G. & Cahen, D. Photovoltaics: perovskite cells roll forward. *Nat. Photonics* **8**, 87–88 (2014).
9. Zhou, H. et al. Interface engineering of highly efficient perovskite solar cells. *Science* **345**, 542–546 (2014).
10. Han, Y. et al. Degradation observations of encapsulated planar $CH_3NH_3PbI_3$ perovskite solar cells at high temperatures and humidity. *J. Mater. Chem. A* **3**, 8139–8147 (2015).
11. Yang, J., Siempelkamp, B. D., Liu, D. & Kelly, T. L. Investigation of $CH_3NH_3PbI_3$ degradation rates and mechanisms in controlled humidity environments using in situ techniques. *ACS Nano* **9**, 1955–1963 (2015).
12. Christians, J. A., Miranda Herrera, P. A. & Kamat, P. V. Transformation of the excited state and photovoltaic efficiency of $CH_3NH_3PbI_3$ perovskite upon controlled exposure to humidified air. *J. Am. Chem. Soc.* **137**, 1530–1538 (2015).
13. Zhao, J. et al. Investigation of the hydrolysis of perovskite organometallic halide $CH_3NH_3PbI_3$ in humidity environment. *Sci. Rep.* **6**, 21976 (2016).
14. Lee, B. et al. Air-stable molecular semiconducting iodosalts for solar cell applications: Cs_2SnI_6 as a hole conductor. *J. Am. Chem. Soc.* **136**, 15379–15385 (2014).
15. Qiu, X. et al. From unstable $CsSnI_3$ to air-stable Cs_2SnI_6: a lead-free perovskite solar cell light absorber with bandgap of 1.48 eV and high absorption coefficient. *Sol. Energy Mater. Sol. Cells* **159**, 227–234 (2017).
16. Zhu, W. et al. Tunable optical properties and stability of lead free all inorganic perovskites ($Cs_2SnI_xCl_{6-x}$). *J. Mater. Chem. A* **6**, 2577–2584 (2018).
17. Lee, B., Krenselewski, A., Baik, S. I., Seidman, D. N. & Chang, R. P. Solution processing of air-stable molecular semiconducting iodosalts, $Cs_2SnI_{6-x}Br_x$, for potential solar cell applications. *Sustain. Energy Fuels* **1**, 710–724 (2017).
18. Jiang, Y., Zhang, H., Qiu, X. & Cao, B. The air and thermal stabilities of lead-free perovskite variant Cs_2SnI_6 powder. *Mater. Lett.* **199**, 50–52 (2017).
19. Guo, F. et al. A two-step dry process for Cs_2SnI_6 perovskite thin film. *Mater. Res. Lett.* **5**, 540–546 (2017).
20. Kapil, G. et al. Investigation of interfacial charge transfer in solution processed Cs_2SnI_6 thin films. *J. Phys. Chem. C* **121**, 13092–13100 (2017).

21. Wang, Q. et al. Scaling behavior of moisture-induced grain degradation in polycrystalline hybrid perovskite thin films. *Energy Environ. Sci.* **10**, 516–522 (2017).
22. Leguy, A. I. M. et al. Reversible hydration of $CH_3NH_3PbI_3$ in films, single crystals, and solar cells. *Chem. Mater.* **27**, 3397–3407 (2015).
23. Lasaga, A. C. & Lüttge, A. A model for crystal dissolution. *Eur. J. Mineral.* **15**, 603–615 (2003).
24. Heinisch, H., Sines, G., Goodman, J. & Kirby, S. Elastic stresses and self-energies of dislocations of arbitrary orientation in anisotropic media: olivine, orthopyroxene, calcite, and quartz. *J. Geophys. Res.* **80**, 1885–1896 (1975).
25. Lasaga, A. C. & Luttge, A. Variation of crystal dissolution rate based on a dissolution stepwave model. *Science* **291**, 2400–2404 (2001).
26. Deegan, R. D. et al. Capillary flow as the cause of ring stains from dried liquid drops. *Nature* **389**, 827–829 (1997).
27. Song, Z. et al. Perovskite solar cell stability in humid air: partially reversible phase transitions in the PbI_2-CH_3NH_3I-H_2O system. *Adv. Energy Mater* **6**, 1600846, 1–7 (2016).
28. Kaltzoglou, A. et al. Optical-vibrational properties of the Cs_2SnX_6 (X = Cl, Br, I) defect perovskites and hole-transport efficiency in dye-sensitized solar cells. *J. Phys. Chem. C.* **120**, 11777–11785 (2016).
29. Huang, B. X., Tornatore, P. & Li, Y.-S. IR and Raman spectroelectrochemical studies of corrosion films on tin. *Electrochim. Acta* **46**, 671–679 (2001).
30. Hickling, G. G. Gravimetric analysis: the synthesis of tin iodide. *J. Chem. Educ.* **67**, 702 (1990).
31. Hao, F., Stoumpos, C. C., Liu, Z., Chang, R. P. & Kanatzidis, M. G. Controllable perovskite crystallization at a gas–solid interface for hole conductor-free solar cells with steady power conversion efficiency over 10%. *J. Am. Chem. Soc.* **136**, 16411–16419 (2014).
32. Schlipf, J. et al. In situ monitoring the uptake of moisture into hybrid perovskite thin films. *J. Phys. Chem. Lett.* **9**, 2015–2021 (2018).
33. Aqvist, J. Ion-water interaction potentials derived from free energy perturbation simulations. *J. Phys. Chem.* **94**, 8021–8024 (1990).
34. Aue, D. H., Webb, H. M. & Bowers, M. T. A thermodynamic analysis of solvation effects on the basicities of alkylamines. An electrostatic analysis of substituent effects. *J. Am. Chem. Soc.* **98**, 318–329 (1976).
35. Lee, S. H. & Rasaiah, J. C. Molecular dynamics simulation of ion mobility. 2. Alkali metal and halide ions using the SPC/E model for water at 25 C. *J. Phys. Chem.* **100**, 1420–1425 (1996).
36. Albinati, A. & Willis, B. The Rietveld method in neutron and X-ray powder diffraction. *J. Appl. Crystallogr.* **15**, 361–374 (1982).
37. Toby, B. H. & Von Dreele, R. B. GSAS-II: the genesis of a modern open-source all purpose crystallography software package. *J. Appl. Crystallogr.* **46**, 544–549 (2013).